

Wettability-independent droplet transport by *Bendotaxis*

Alexander T. Bradley, Finn Box, Ian J. Hewitt and Dominic Vella¹

¹*Mathematical Institute, University of Oxford, Woodstock Rd, Oxford OX2 6GG, United Kingdom*

(Dated: March 12, 2019)

We demonstrate *bendotaxis*, a novel mechanism for droplet self-transport at small scales. A combination of bending and capillarity in a thin channel causes a pressure gradient that, in turn, results in the spontaneous movement of a liquid droplet. Surprisingly, the direction of this motion is always the same, regardless of the wettability of the channel. We use a combination of experiments at a macroscopic scale and a simple mathematical model to study this motion, focussing in particular on the time scale associated with the motion. We suggest that *bendotaxis* may be a useful means of transporting droplets in technological applications, for example in developing self-cleaning surfaces, and discuss the implications of our results for such applications.

PACS numbers: 47.55.nb,46.25.-y,46.35.+z

Control and transport of liquid droplets on small scales, where surface forces dominate, is of critical importance in applications including microfluidics, microfabrication and coatings [1–5]. Active processes including gradients in temperature [6, 7], applied electric potentials [8] and mechanical actuation [9] have been used successfully to generate such fine scale control. Recently, however, there has been growing interest in generating droplet motion passively. This can be achieved using a fixed geometry, in which droplets move in response to tapering [10–14]. When the geometry is responsive (e.g. with deformable boundaries), however, more possibilities open up, including *durotaxis* [1] and *tensotaxis* [15], which rely on gradients in stiffness and strain of an underlying soft substrate, respectively, to control motion. Here we introduce a novel, passive droplet transport mechanism that takes advantage of the capillary-induced bending of a narrow channel whose walls are slender and hence deformable; we term this motion *bendotaxis*. Importantly, we shall demonstrate that the direction of *bendotaxis* is independent of wettability. This is in contrast to *durotaxis*, in which wetting and non-wetting droplets have been reported to move in opposite directions [16].

Figure 1(a) illustrates the mechanism behind *bendotaxis*: two, initially parallel, bendable walls are clamped at one end and free at the other, forming a two-dimensional channel. If a wetting droplet is introduced between the walls, the negative Laplace pressure deflects the walls inwards. The deformation is larger at the meniscus closer to the free end (referred to as x_+) than at the clamped end (x_-). The pressure is therefore more negative at x_+ than at x_- ; the resulting pressure gradient drives the droplet towards the free end. Provided the contact angles remain the same and the beams do not touch, this motion will continue until the droplet reaches the free end. For a non-wetting droplet introduced into the channel, the Laplace pressure is positive, pushing the beams away from one another but the resulting pressure gradient is again negative, driving the droplet towards the free end.

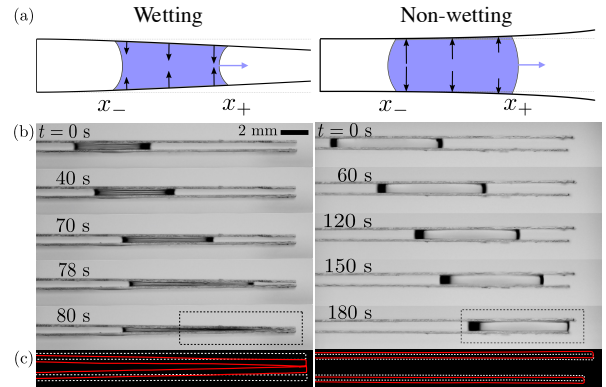


FIG. 1: (a) Schematic diagrams explain the mechanism behind *bendotaxis* for wetting (left) and non-wetting (right) drops: black arrows indicate the sign and magnitude of the Laplace pressure within the drop; purple arrows show the direction of decreasing pressure and hence motion. (b) Experimental demonstration of *bendotaxis* for a wetting silicone oil droplet (left) and a non-wetting water droplet (right), each between initially parallel, yet deformable, SLIPS. While the deformation of the channel is different in each case, the direction of droplet motion is the same. (c) Comparison of final channel shape (red lines) with the initial channel shape (dotted white lines) for the section highlighted by the dashed box in (b).

This mechanism is reproducible in a simple laboratory experiment. We fabricated channels using a rigid separator and glass coverslips. Figure 1(b) shows time-series of a wetting silicone oil droplet and of a non-wetting water droplet in such a channel. In both cases, the droplets move towards the free end of the channel. To observe the deflection of the coverslips, we compare their shapes in the final configuration with those prior to the introduction of the droplet (fig. 1(c)). In the wetting case, both coverslips are deflected inwards, while in the non-wetting case both are deflected outwards, in accord with our physical description. The observed deflections also provide evidence that motion is not simply caused by the weight of the droplet, which would cause the lower cov-

erslip to deflect downwards in both cases. (Our neglect of gravity is justified in [47].)

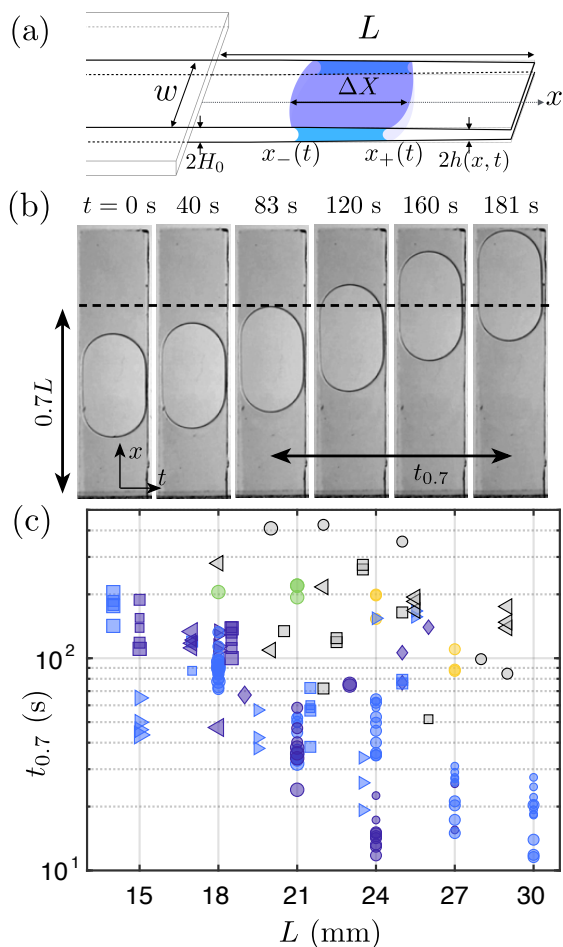


FIG. 2: (a) Schematic of a droplet in a flexible channel of undeformed wall separation $2H_0$, width w and length L , with menisci positioned at $x = x_-(t)$ and $x = x_+(t)$. (b) Top view of a droplet of V50 silicone oil (channel length $L = 18$ mm, width $w = 5$ mm, wall separation $2H_0 = 310 \mu\text{m}$, thickness $b = 300 \mu\text{m}$ and droplet volume $V = 10 \mu\text{L}$). Although the droplet spans the width of the channel, it is not precisely two-dimensional. We present data for $t_{0.7}$: the time between the events $x_+/L = 0.7$ and $x_+/L = 1$, which corresponds to the time between the fourth and sixth images here. (c) Raw experimental measurements of $t_{0.7}$, for different beam lengths, L . Data are shown for droplets of wetting silicone oil and a non-wetting water-glycerol mix; droplet type is encoded as in fig. 3. Different shapes encode channel wall separation as follows: $2H_0 = 310 \mu\text{m}$ (\triangleright), $360 \mu\text{m}$ (\triangleleft), $430 \mu\text{m}$ (\square), $540 \mu\text{m}$ (\circ), $630 \mu\text{m}$ (\diamond). The size of each point encodes the approximate fraction of the channel taken by the droplet ($\hat{V} = \Delta X/L$), with bins corresponding to $\hat{V} < 0.25$, $0.25 \leq \hat{V} < 0.35$, $0.35 \leq \hat{V} < 0.45$ and $\hat{V} \geq 0.45$.

To gain insight into the dynamics of bendotaxis we performed a series of more detailed experiments: sections of borosilicate glass coverslips (Agar Scientific, Young's modulus $E = 63$ GPa, thickness $160 \mu\text{m} \leq$

$b \leq 310 \mu\text{m}$ ($\pm 5 \mu\text{m}$), width $w = 5 \pm 0.5$ mm) were first treated (see below) before being clamped with a separation $310 \mu\text{m} \leq 2H_0 \leq 630 \mu\text{m}$ ($\pm 5 \mu\text{m}$) to create an open-ended channel, as in fig. 2(a). The channel length $14 \text{ mm} \leq L \leq 30 \text{ mm}$ (± 0.25 mm) is controlled by changing the clamping position (while maintaining a relatively long clamped section to ensure there is no intrinsic tapering, which would alter the dynamics [11, 13, 17]).

The treatment of the glass and the droplets used depended on the required wetting conditions: for the non-wetting case, the walls were sprayed with a commercial hydrophobic spray (Soft-99, Japan) and dip-coated with silicone oil V5 (Sigma-Aldrich, USA) forming a slippery lubricant-infused porous surface (SLIPS) [18–20, 47]. Droplets were formed from a water-glycerol mix (70% water by weight, dynamic viscosity $\mu = 36 \pm 5$ mPa s, surface tension $\gamma = 67$ mN m $^{-1}$); this combination of drop and lubricant liquids ensures a large advancing contact angle ($\theta_a = 102 \pm 2^\circ$ [47]), low hysteresis (receding angle $\theta_r = 100 \pm 2^\circ$) and a large enough drop:lubricant viscosity ratio that viscous dissipation occurs primarily within the droplet [21, 47].

In the wetting case, we pre-wetted the glass with silicone oil (pre-wetting was performed on both bare glass, as well as with glass pre-treated by hydrophobic spray to better retain the wetting film; we find no difference between these two cases in our experimental data [47]). Droplets of silicone oils V50, V100, V350 and V500, were used to vary the dynamic viscosity in the range $48 \leq \mu \leq 480$ mPa s $\pm 5\%$ while maintaining $\gamma = 22$ mN m $^{-1}$. These droplets perfectly wet the pre-wetted glass but form a capillary bridge with well-defined menisci.

The droplet volume was systematically varied in the range $10 \pm 0.5 \mu\text{L} \leq V \leq 25 \pm 0.5 \mu\text{L}$, leading to different initial droplet lengths $\Delta X = x_+(0) - x_-(0)$ and, hence, different relative volumes $\hat{V} = \Delta X/L$ (constant in each experiment). The wall separation at the free end is enforced to be $2H_0$ during droplet deposition but removed shortly after, which corresponds to $t = 0$; in this brief period immediately following deposition, droplet motion is negligible [5, 47]. The experiment is photographed from above, as in fig. 2(b), and the position of the leading meniscus, $x_+(t)$, is recorded and tracked using image analysis software in MATLAB. (Note that the droplet volumes V were chosen so that the drop spans the width w of the channel, becoming effectively two-dimensional, fig. 2(b).)

To quantify the time scale of motion in a reproducible manner (independent of the initial droplet position), we measure the time, t_X , taken for the droplet to pass from $x_+/L = X$ to the free end $x_+/L = 1$. This quantity is approximately independent of the initial condition, provided inertia is negligible. Here we present results for $X = 0.7$, which is arbitrary but covers a significant portion of the motion for which beam bending occurs over a

length comparable to L (a fact used in the following scaling arguments), whilst still allowing most experiments to be included.

Raw measurements of $t_{0.7}$ are presented in fig. 2(c), and indicate a strong dependence on both channel geometry and droplet viscosity. To gain theoretical insight, we first consider a scaling argument assuming a small relative volume, $\hat{V} \ll 1$, which captures the combination of elasticity and capillarity involved. Droplet motion is driven by the Laplace pressure change that results from droplet-induced tapering of the channel (we assume a constant surface tension γ and contact angle θ at the leading and rear menisci and neglect the surface tension from the sides, shown to be relatively unimportant in a similar situation [22]). In a narrow channel, the pressure change across the droplet due to a tapering angle α can be approximated as $\Delta P \sim \alpha \gamma \cos \theta \Delta X / H_0^2$. Since the channel walls bend over a length comparable to L (provided the drop is relatively far from the clamp), but are only subject to a Laplace pressure over the length of the drop, linear beam theory [23] suggests that $\alpha \sim \gamma \cos \theta L^2 \Delta X / B H_0$. (Here $B = E b^3 / 12$ is the bending stiffness of the wall per unit width [24, 47].) Therefore, the pressure gradient over the (small) droplet is estimated as

$$\frac{\partial P}{\partial x} \sim \frac{L^2 \gamma^2 \cos^2 \theta \Delta X}{H_0^3 B}. \quad (1)$$

Lubrication theory [25] provides the timescale for a droplet of viscosity μ to move along the length of the beams as $\tau \sim \mu L / (H_0^2 P_x)$. When considered relative to a capillary timescale $\tau_c = \mu L^2 / (|\gamma \cos \theta| H_0)$, this yields

$$\frac{\tau}{\tau_c} = \frac{\tau |\gamma \cos \theta| H_0}{\mu L^2} \sim \frac{B}{|\gamma \cos \theta| \Delta X} \frac{H_0^2}{L^3}. \quad (2)$$

The scaling (2) provides a reasonable collapse of the experimental data for all of the wetting data, see fig. 3 and fig. S1 [47]. However, the non-wetting experiments show two families with a similar scaling trend but modified prefactors, which may be due to a change in the effective value of $|\gamma \cos \theta|$ between measurements made on a single SLIPS and experiments in a narrow channel. A possible cause for such a change in the driving Laplace pressure is a thin oil layer ‘cloaking’ the droplet [26]. Quantifying this is beyond the scope of the present study, but we note that the discrepancy in prefactor would be eliminated by a relatively small change in the effective contact angle of $\lesssim 7^\circ$.

For moderate to large values of the abscissa in fig. 3 we observe the linear scaling of (2) (valid for $\hat{V} \ll 1$). However, at smaller values (larger \hat{V}) the linear scaling appears to break down. To go beyond this scaling argument and determine the effect of finite droplet volumes \hat{V} , we formulate a detailed mathematical model. Combining lubrication theory and linear beam theory (and

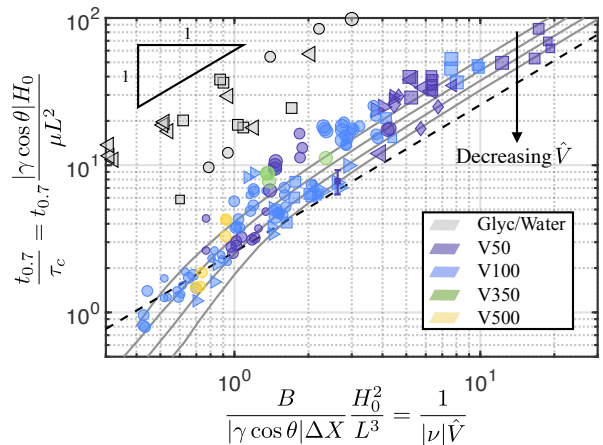


FIG. 3: Collapse of experimental data when rescaled according to (2). Points correspond to experimental observations (with volume and wall separation encoded by point size and shape, respectively, as in fig. 2; droplet type is encoded by color, as indicated in the legend). The single set of error bars extends one standard deviation away from a particular data point, computed from 20 measurements, and is similar for each experiment [47]. Solid curves show results from numerical solutions of (3)–(5) with $\hat{V} = 0.5, 0.4, 0.3$ and $\hat{V} = 0.2$. Also plotted is the asymptotic result (7) (black dashed line), valid for $\hat{V} \ll 1$ (corresponding to the upper right corner of this plot).

neglecting the weight and tension within the beam) leads to a nonlinear PDE for the deformed shape of the beams $h(x, t)$ within the wetted region [27–29]:

$$\frac{\partial h}{\partial t} = \frac{B}{3\mu} \frac{\partial}{\partial x} \left[h^3 \frac{\partial^5 h}{\partial x^5} \right], \quad x_-(t) < x < x_+(t). \quad (3)$$

The shape of the channel wall out of contact with the droplet satisfies $\partial^4 h / \partial x^4 = 0$ and depend on time only through the meniscus positions. At each meniscus we require continuity of shape, slope, moments and shear force, consistent with the assumption of a small aspect ratio, $H_0 / L \ll 1$, used in lubrication theory [28]. The pressure jump between dry and wet portions of the beam is due to the Laplace pressure at the meniscus, so that

$$B \frac{\partial^4 h}{\partial x^4} \Big|_{x=x_m} = -\frac{\gamma \cos \theta}{h(x_m, t)}, \quad x_m = x_-, x_+. \quad (4)$$

As before, we have assumed that the contact angles at the advancing and receding menisci are equal and constant. On the timescales considered here, evaporation is negligible [47] conservation of mass then requires

$$\frac{dx_m}{dt} = -\frac{B h^2}{3\mu} \frac{\partial^5 h}{\partial x^5} \Big|_{x=x_m}, \quad x_m = x_-, x_+, \quad (5)$$

We apply clamped boundary conditions at $x = 0$, while the end $x = L$ is free, i.e. $h(0, t) = H_0$, $h_x(0, t) = 0$, and $h_{xx}(L, t) = h_{xxx}(L, t) = 0$. The problem is closed by

specifying initial conditions for the beam shape, $h(x, 0) = H_0$, and the meniscus positions $x_-(0) = x_-^0$, $x_+(0) = x_+^0$.

Asymptotic analysis of the problem (3)-(5) for $\hat{V} \ll 1$ shows that the beam deflection is small and that the drop length is approximately constant throughout the motion [47]. The evolution of the meniscus positions are then governed by the ODEs

$$\frac{dx_m}{dt} = \frac{\gamma^2 \cos^2 \theta \Delta X}{6B\mu H_0} x_m^2, \quad x_m = x_-, x_+. \quad (6)$$

The ODE for $x_+(t)$ may be solved to give the time t_X taken to move from $x_+/L = X$ to $x_+/L = 1$ as

$$\frac{t_X}{\tau_c} = \frac{6(1-X)}{X} \frac{B}{|\gamma \cos \theta| \Delta X} \frac{H_0^2}{L^3}. \quad (7)$$

Eqn (7) confirms the scaling result (2) and provides the appropriate pre-factor, which, with $X = 0.7$, corresponds to the black dashed line in fig. 3.

To facilitate numerical solutions of the full problem (3)-(5), we non-dimensionalize axial lengths by L , the beam deformation by H_0 and time by the capillary timescale τ_c , introduced earlier. In addition to the relative volume \hat{V} , we identify a further dimensionless parameter

$$\nu = \frac{L^4 \gamma \cos \theta}{H_0^2 B}, \quad (8)$$

which represents the ability of the droplet surface tension to bend the channel walls. We refer to the parameter ν as a channel ‘bendability’, though it is also related to the reciprocal of the elastocapillary number [5]. Note that wetting drops have $\nu > 0$ while non-wetting drops have $\nu < 0$, consistent with the sign of the pressure in equation (4).

The problem is fully specified by the values of ν , \hat{V} , and the initial condition x_+^0/L , and can be solved numerically in MATLAB using the method of lines [30, 47]. The numerical solution determines the time taken for a droplet starting with $x_+^0/L = 0.7$ to reach $x_+/L = 1$ for different values of \hat{V} and ν i.e. we may write

$$\frac{t_{0.7}}{\tau_c} = f(\nu, \hat{V}). \quad (9)$$

The scaling law (2) shows that $f(\nu, \hat{V}) \sim (\nu \hat{V})^{-1}$ in the limit $\hat{V} \ll 1$. The numerically-determined values of $t_{0.7}/\tau_c$ are plotted in fig. 3 for several values of \hat{V} (spanning the experimentally realized range). These results suggest that some of the discrepancy between experiments and the scaling prediction (7) are accounted for by the finite value of \hat{V} . The neglect of some physical aspects may also result in deviation of experimental results from the numerical solutions; surface defects, the presence of gravity and surface tension acting along the sides

will, for example, influence the dynamics. Whilst we expect these to be relatively unimportant [47], they will introduce ‘noise’ into experimental results not accounted for by the model.

Numerical solutions of the dimensionless version of (3)-(5) yield the values of $f(\nu, \hat{V})$, which are shown in a color-map in fig. 4 with, schematics of the deformed channel shape. This demonstrates that, for fixed relative droplet volume \hat{V} , the time $t_{0.7}$ decreases as the absolute bendability $|\nu|$ increases (e.g. by decreasing the wall thickness b , or Young’s modulus E). However, this is to be weighed against the possibility of the edges of the walls touching and trapping wetting drops indefinitely (see upper curve in fig. 4).

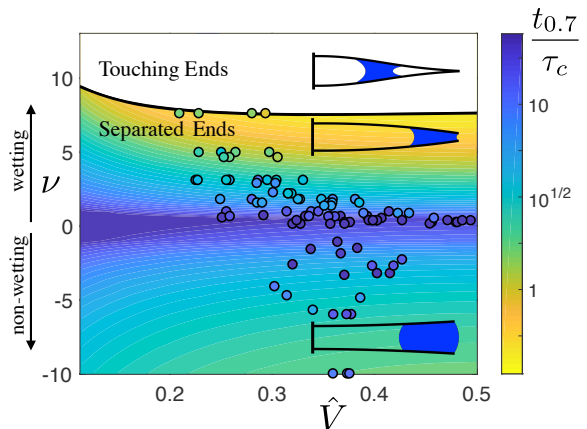


FIG. 4: Influence of dimensionless droplet volume, \hat{V} , and channel bendability, ν , on the time taken to traverse the final 30% of the channel, $t_{0.7}/\tau_c$. Numerical results are shown by varying color, while the bold black curve indicates parameter values for which the edges of the channel touch during the motion, trapping the droplet. (Note that the position of this curve depends on the initial condition; here $x_+^0/L = 0.6$.) Positive bendability, $\nu > 0$, corresponds to wetting drops, while $\nu < 0$ corresponds to non-wetting drops; when $\nu = 0$, the channel is effectively rigid and the droplet remains stationary. Schematics illustrate typical configurations, and filled circles correspond to the experimental data presented in figures 2 and 3; the outliers with $\nu < 0$ are in the slow non-wetting regime.

In this Letter, we have shown that a drop placed into a channel with deformable, but initially parallel, walls creates its own tapered channel, driving itself towards the free end, independent of the droplet wettability. We suggest that this universality of motion may find application in self-cleaning surfaces able to remove macroscopic contaminants [31]. In particular, surfaces are often textured at a microscopic scale to reduce adhesion and increase droplet mobility [32, 33]. However, these properties can be impaired if liquid impregnates the texture [34]. Tapering the texture has been suggested to reduce the internal fogging of some surfaces [35], effectively expelling the soiling droplets automatically, but only works if these

droplets are themselves non-wetting. A similar role has been suggested for the hairy coating on the legs of water-walking arthropods such as *Gerris Regimis* [36]. Here we have shown that under bendotaxis both wetting and non-wetting drops move to the free end of a rectangular channel, where they might naturally evaporate, be knocked off or even jump from the surface [37]. Rapid motion occurs for large values of the bendability, at the risk of trapping wetting droplets (fig. 4).

There remain many features of the system (including contact angle hysteresis three-dimensional geometry, and the behavior of the droplet at the end of the channel) that might complicate the picture of bendotaxis presented here. However, these complications may also provide further opportunities for passive droplet control with more sensitivity: for example, by tapering the undeformed channels slightly, we expect there would be a range of values of the bendability for which droplets would actually move towards the clamped end.

This research was supported by the European Research Council under the European Horizon 2020 Programme, ERC Grant Agreement no. 637334 (DV) and the John Fell Fund, Grant no. BKD00020 (FB).

-
- [1] R. W. Style, Y. Che, S. J. Park, B. M. Weon, J. H. Je, C. Hyland, G. K. German, M. P. Power, L. A. Wilen, J. S. Wettlaufer, et al., *Proc. Natl. Acad. Sci.* **110**, 12541 (2013).
- [2] T. M. Squires and S. R. Quake, *Rev. Mod. Phys.* **77**, 977 (2005).
- [3] M. Srinivasarao, D. Collings, A. Philips, and S. Patel, *Science* **292**, 79 (2001).
- [4] P.-G. de Gennes, F. Brochard-Wyart, and D. Quéré, *Capillarity and Wetting Phenomena: Drops, Bubbles, Pearls, Waves* (Springer-Verlag New York, 2004).
- [5] C. Mastrangelo and C. Hsu, *J. Microelectromech. Sys.* **2**(1), 33 (1993).
- [6] T. S. Sammarco and M. A. Burns, *React. Kinet. Catal.* **45**, 350 (1999).
- [7] V. Pratap, N. Moumen, and R. S. Subramanian, *Langmuir* **24**, 5185 (2008).
- [8] F. Mugele and J.-C. Baret, *J. Phys. Condens. Matter* **17**, R705 (2005).
- [9] M. Prakash, D. Quéré, and J. W. M. Bush, *Science* **320**, 931 (2008).
- [10] S.-H. Kim and D. A. Weitz, *Angew. Chem.* **123**, 8890 (2011).
- [11] E. Reyssat, *J. Fluid Mech.* **748**, 641 (2014).
- [12] C. Lv, C. Chen, Y.-C. Chuang, F.-G. Tseng, Y. Yin, F. Grey, and Q. Zheng, *Phys. Rev. Lett.* **113**, 026101 (2014).
- [13] P. Renvoisé, J. W. M. Bush, M. Prakash, and D. Quéré, *Europhys. Lett.* **86**, 64003 (2009).
- [14] J. H. Guan, É. Ruiz-Gutiérrez, B. B. Xu, D. Wood, G. McHale, R. Ledesma-Aguilar, and G. G. Wells, *Soft Matter* **13**, 3404 (2017).
- [15] J. Bueno, Y. Bazilevs, R. Juanes, and H. Gomez, *Extreme Mech. Lett.* **13**, 10 (2017).
- [16] J. Bueno, Y. Bazilevs, R. Juanes, and H. Gomez, *Soft Matter* **14**, 1417 (2018).
- [17] J.-B. Gorce, I. J. Hewitt, and D. Vella, *Langmuir* **32**, 1560 (2016).
- [18] T.-S. Wong, S. H. Kang, S. K. Y. Tang, E. J. Smythe, B. D. Hatton, A. Grinthal, and J. Aizenberg, *Nature* **477**, 443 (2011).
- [19] J. D. Smith, R. Dhiman, S. Anand, E. Reza-Garduno, R. E. Cohen, G. H. McKinley, and K. K. Varanasi, *Soft Matter* **9**, 1772 (2013).
- [20] J. T. Luo, N. R. Galdi, J. H. Guan, G. McHale, G. G. Wells, and Y. Q. Fu, *Phys. Rev. Applied* **7**, 014017 (2017).
- [21] A. Keiser, L. Keiser, C. Clanet, and D. Quéré, *Soft Matter* **13**, 6981 (2017).
- [22] H.-M. Kwon, H.-Y. Kim, J. Puëll, and L. Mahadevan, *J. Appl. Phys.* **103**, 093519 (2008).
- [23] P. Howell, G. Kozyreff, and J. Ockendon, *Applied Solid Mechanics*, Cambridge Texts in Applied Mathematics (Cambridge University Press, 2009).
- [24] B. Audoly and Y. Pomeau, *Elasticity and Geometry* (Oxford University Press, 2010).
- [25] L. G. Leal, *Advanced Transport Phenomena: Fluid Mechanics and Convective Transport Processes* (Cambridge University Press, 2007).
- [26] F. Schellenberger, J. Xie, N. Encinas, A. Hardy, M. Klapper, P. Papadopoulos, H.-J. Butt, and D. Vollmer, *Soft Matter* **11**, 7617 (2015).
- [27] J. M. Aristoff, C. Duprat, and H. A. Stone, *Int. J. Nonlin. Mech.* **46**, 648 (2011).
- [28] M. Taroni and D. Vella, *J. Fluid Mech.* **712**, 273 (2012).
- [29] C. Duprat, J. M. Aristoff, and H. A. Stone, *J. Fluid Mech.* **679**, 641 (2011).
- [30] W. Schiesser, *The Numerical Method of Lines: Integration of Partial Differential Equations* (Academic Press, 1991).
- [31] C. Neinhuis and W. Barthlott, *Ann. Bot.* **79**, 667 (1997).
- [32] J. Bico, C. Marzolin, and D. Quéré, *EPL* **47**, 220 (1999).
- [33] D. Quéré, *Rep. Prog. Phys.* **68**, 2495 (2005).
- [34] Y.-T. Cheng and D. E. Rodak, *Appl. Phys. Lett.* **86**, 144101 (2005).
- [35] T. Mouterde, G. Lehoucq, S. Xavier, A. Checco, C. T. Black, A. Rahman, T. Midavaine, C. Clanet, and D. Quéré, *Nat. Mater.* **16**, 658 (2017).
- [36] Q. Wang, X. Yao, H. Liu, D. Quéré, and L. Jiang, *Proc. Natl. Acad. Sci.* **112**, 9247 (2015).
- [37] K. M. Wisdom, J. A. Watson, X. Qu, F. Liu, G. S. Watson, and C.-H. Chen, *Proc. Natl. Acad. Sci.* **110**, 7992 (2013).
- [38] Schott AG, *Borosilicate glass properties*, online; accessed 27-September-2018, URL www.schott.com/d/tubing/9a0f5126-6e35-43bd-bf2a-349912caf9f2/schott-algae-brochure-borosilicate.pdf.
- [39] K. Takamura, H. Fischer, and N. R. Morrow, *J. Petr. Sci. Engng* **98-99**, 50 (2012).
- [40] C. A. Schneider, W. S. Rasband, and K. Eliceiri, *Nature Methods* **9** (2012).
- [41] Y. Yuan and T. R. Lee, in *Surface science techniques* (Springer, 2013), pp. 3-34.
- [42] T. Onda, S. Shibuichi, N. Satoh, and K. Tsujii, *Langmuir* **12**, 2125 (1996).
- [43] J. Canny, *IEEE Trans. Pattern Anal. Mach. Intell.* **8**, 679 (1986).

- [44] H. Hu and R. G. Larson, *J. Phys. Chem. B* **106**, 1334 (2002).
- [45] L. Zhornitskaya and A. L. Bertozzi, *SIAM J. Numer. Anal.* **37**, 523 (2000).
- [46] L. F. Shampine, *ACM Trans. Math. Softw.* **33**, 26 (2007).
- [47] See Supplementary Information, which includes refs [38–46], for details of the experimental procedure, asymptotic analysis and numerical techniques.